

# Temporal monitoring of subglacial volcanoes with TanDEM-X – Application to the 2014–2015 eruption within the Bárðarbunga volcanic system, Iceland



Cristian Rossi <sup>\*</sup>, Christian Minet, Thomas Fritz, Michael Eineder, Richard Bamler

Remote Sensing Technology Institute, German Aerospace Center (DLR), D-82234 Oberpfaffenhofen, Germany

## ARTICLE INFO

### Article history:

Received 18 September 2015  
Received in revised form 1 April 2016  
Accepted 8 April 2016  
Available online xxxx

### Keywords:

TanDEM-X  
DEM accuracy  
Snow  
Ice  
Volcanoes  
Bárðarbunga  
Holuhraun

## ABSTRACT

On August 29, 2014, a lava eruption commenced in the Holuhraun plain, north-east of the Bárðarbunga caldera in Iceland. The eruption ended on February 27, 2015, thus lasting for a period of about 6 months. During these months the magma chamber below the caldera gradually deflated, feeding the eruption and causing the rare event of a slow caldera collapse. In this scenario, TanDEM-X remote sensing data are of particular interest. By producing medium-high resolution and accurate elevation models of the caldera, it is possible to evaluate volume losses and topographical changes to increase the knowledge about the ongoing activity. In particular, five TanDEM-X bistatic acquisitions have been commanded between August 01, 2014 and November 08, 2014, two of them before the volcanic eruption and three of them during the event. Additionally, to fully cover the volcanic activity, the lava field 48 km north-east of the caldera has also been monitored. In the first part of the paper, the expected elevation accuracy is studied on two levels. Absolute and relative height accuracies are analyzed by inspecting the X-band signal propagation into snow and by investigating the impact of the main geometrical system parameters and the local geomorphology. In the second part of the paper, the analysis is applied to the Bárðarbunga volcanic system, including a validation performed using complementary altimeter data. The main geophysical outcome is the accurate temporal height tracking of the entire caldera and the glacial volcanic system. The measured volume loss at the caldera location is about 1 billion cubic meters in two months with an average rate of subsidence of nearly 50 cm/day. These numbers confirm other independent sources and can be compared to lava volume measurements. Finally, the last segment of the dyke that propagated from the Bárðarbunga caldera to the Holuhraun lava field is mapped and a graben structure with a width of up to 1 km and a sinking of a few meters is reported.

© 2016 The Authors. Published by Elsevier Inc. This is an open access article under the CC BY-NC-ND license (<http://creativecommons.org/licenses/by-nc-nd/4.0/>).

## 1. Introduction

Volcanoes need the continuous monitoring of the environment in which they are located in order to ensure safety in the event of volcanic hazards. The main volcanic hazards in Iceland were reported by Gudmundsson, Larsen, Höskuldsson, and Gylfason (2008). Jökulhlaups, i.e. outburst meltwater floods, are common hazards (Björnsson, 2003). For instance, the Katla jökulhlaup from the 1918 eruption caused an inundation of about 800 km<sup>2</sup>, being one of the largest in Iceland (Tómasson, 1996). Bárðarbunga is located under Vatnajökull, the largest glacier in Iceland. Floods forming on Vatnajökull ice cap are well-known and studied, especially from the Grímsvötn volcano (Gudmundsson, Björnsson, & Pálsson, 1995), nearly 30 km south-east of Bárðarbunga, and the Skaftá ice cauldrons (Old, Lawler, & Snorrason, 2005), approximately 17 km south of Bárðarbunga. Lava flows are potentially dangerous for local populations when they occur close to inhabited areas, or are exceptionally voluminous, such as those generated during

the 1783–1784 Laki eruption (Thordarson & Self, 2003). Tephra fallout is also a major hazard, e.g. Litla-Hérað was devastated by tephra fall during the Öræfajökull eruption in 1362 (Larsen, Gudmundsson, & Björnsson, 1998). The most recent 2010 Eyjafjallajökull eruption was also remarkably hazardous, affecting north Atlantic flight tracks (Gertisser, 2010) and depositing tephra over several European countries (Stevenson et al., 2012). The primary hazard associated with the recent Bárðarbunga/Holuhraun eruption was the emission of gas (sulphur dioxide) from the lava field (Gíslason, Stefánsdóttir, Pfeffer, Barsotti, & Jóhannsson, 2015), however throughout this activity – and especially during the initial propagation of the dyke – there was also the possibility of a major jökulhlaup if an additional eruption site were to open up beneath the Vatnajökull ice-cap. The eruption has been extensively and in near real-time studied by the Institute of Earth Sciences at the University of Iceland and by the Icelandic Met Office, who provided reports on an almost daily-basis on their websites (Icelandic Met Office, 2014; Institute of Earth Science, 2014).

Among remote sensing technologies, Synthetic Aperture Radar (SAR) is of great help due to the ability of these systems to collect

<sup>\*</sup> Corresponding author.

E-mail address: [cristian.rossi@dlr.de](mailto:cristian.rossi@dlr.de) (C. Rossi).

imagery independent of solar illumination and cloud cover. A large number of InSAR studies have been undertaken at volcanoes all around the world. The primary techniques employed for volcano monitoring are differential Interferometric SAR (dInSAR), aimed at revealing surface displacements, e.g. Amelung, Jónsson, Zebker, & Segall, 2000; Hooper, Prata, & Sigmundsson, 2012; Jónsson et al., 1999; Sigmundsson et al., 2010; Sigmundsson et al., 2015, and multi-image InSAR techniques such as Persistent Scatterer Interferometry (PSI) and Small Baseline Interferometry (SBAS), to detect temporal variations in ground displacements, e.g. (Colesanti, Ferretti, Prati, & Rocca, 2003; Hooper, Segall, & Zebker, 2007; Zhong & Dzurisin, 2014). InSAR is used in this paper as an instrument to generate Digital Elevation Models (DEMs). A German mission has been established in 2010 for this purpose and named TanDEM-X (TerraSAR-X add-on for Digital Elevation Measurement) (Krieger et al., 2007). The objective of the mission is to generate a global DEM at 12 m posting with an absolute vertical error below 10 m. As the mission name suggests, the basic operation was to add a satellite to the existing TerraSAR-X satellite and, by flying in close formation, to create a spaceborne bistatic interferometer. The absence of temporal decorrelation, i.e. temporal changes yielding inaccurate elevation models, permits the generation of DEMs with high accuracy standards. The mission operation is rather flexible and allows scientific acquisitions beyond the nominal ones required for the global DEM generation (Hajnsek & Busche, 2014). With this flexibility, stacks of bistatic acquisitions can be studied and temporal DEM series can be generated.

The interest in temporal elevation maps is high. Every mapped patch on Earth can be described in terms of elevation. Changes can be investigated and difference maps produced. Various terrain types have been already temporally investigated with TanDEM-X. For instance, changes at glaciers (Rott et al., 2014), growth of agricultural fields (Rossi & Erten, 2015; Erten, Rossi, & Yuzugullu, 2015), deforestation (Schlund, von Poncet, Hoekman, Kuntz, & Schmuilius, 2014) and urban growth studies (Taubenböck et al., 2012) are among successful examples of TanDEM-X temporal data usage. Volcano topographical changes have been also reported with TanDEM-X. Lava discharge rates at Kilauea Volcano in Hawai'i (USA), volumetric changes at the lava dome of Merapi volcano in Indonesia and lava flow volumes at Nyamulagira volcano in D.R. of Congo have been investigated in Poland (2014); Kubanek et al. (2015), and Albino, Smets, d'Oreye, and Kervyn (2015), respectively.

The application considered in this paper is the 2014–2015 eruption within the Bárðarbunga volcanic system. A small fissure opened up in the Holuhraun plain on August 29, 2014, and the eruption lasted a few hours. The main fissure eruption commenced on August 31, 2014, and lasted for 6 months. The unrest started mid-August 2014, with an intense seismic swarm (Institute of Earth Science, 2014). This was the largest lava forming eruption to occur in Iceland since Laki (1783–1784). A total of  $1.6 \pm 0.3 \text{ km}^3$  of lava was produced during the Holuhraun eruption covering an area of  $84.1 \pm 0.6 \text{ km}^2$  (Gíslason et al., 2015). Through the combined use of InSAR and GPS measurements, the dyke propagation was also modelled and a magma flow rate of  $260 \text{ m}^3/\text{s}$  was reported (Sigmundsson et al., 2015). During these months, the Bárðarbunga caldera slowly collapsed, which is a rare event in Iceland (the previous caldera collapse in Iceland is dated 1875) (Larsen, Gudmundsson, Einarsson, Óladóttir, & Thordarson, 2015; Riel et al., 2015). The University of Iceland acquired elevation data with a radar altimeter in C-band (Gudmundsson, Höganadóttir, Kristinsson, & Guðbjörnsson, 2007) for specific tracks over the caldera during and after the eruption (Gudmundsson, Jónsdóttir, & Roberts, 2015).

TanDEM-X data are used in this paper as an instrument to reveal the topographical changes that occurred to the volcanic system during the eruption. A total of five acquisitions, two before the eruption started and three during the event, are employed for the DEM generation. The acquisitions fully cover the Bárðarbunga caldera and the southern part of this volcanic system. The footprint of the data stack and the caldera outline are presented in Fig. 1. This figure shows the topography of Iceland and is generated by mosaicking TanDEM-X DEM tiles (Gruber et al., 2015). In addition, the lava field topographical changes are also investigated with two complementary TanDEM-X acquisitions over the Holuhraun plain.

Before deriving volcanological parameters, the accuracy of the DEMs is investigated. DEM accuracy depends on the mapped environment. To provide two opposite examples, a water surface cannot be accurately mapped with TanDEM-X in standard configuration since water decorrelates in a fraction of a second, whereas exposed rocks can be mapped with a very high accuracy (Bamler & Hartl, 1998). Our test site is rather particular since the Bárðarbunga caldera is composed of a layer of 600–800 m thick ice above the caldera's surface (Larsen et al., 2015). Here, the SAR wave penetration into materials can play a big role since the measured height depends on the penetration depth (Richards, 2009). The dielectric properties of the caldera ice cap

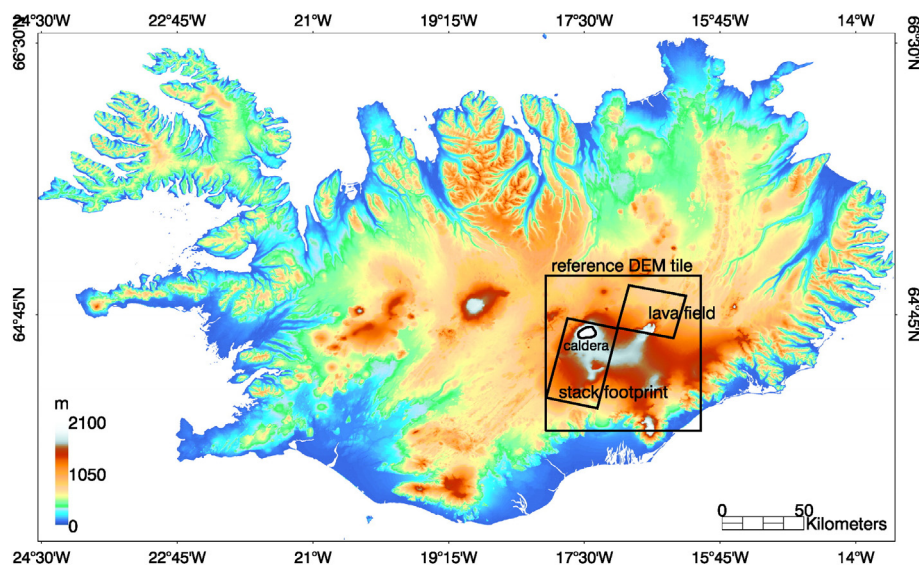


Fig. 1. Footprints of the TanDEM-X acquisitions over the Bárðarbunga caldera and the Holuhraun lava field. This figure shows the topography of Iceland and is generated by mosaicking TanDEM-X DEM tiles. The reference TanDEM-X DEM tile, used for calibration purposes within this study, is also highlighted.

must then be taken into account, together with the various system parameters, i.e. the signal bandwidth and the incidence angle. Details on the overall impacts of snow and SAR system variations on DEM uncertainty are presented in Section 2 and Section 3, respectively. The description of the TanDEM-X dataset and its calibration is outlined in Section 4 and the temporal analysis is presented in Section 5. The radar altimeter elevation measurements are taken as reference for the comparison in Section 6. The subglacial graben structure and the lava path in the Holuhraun plain are analyzed in Section 7. Finally, Section 8 summarizes and concludes the paper.

## 2. Snow impact on DEM uncertainty

Even though, with a human eye, a snow or ice cap looks like a quite easy terrain to map due to the absence of evident height discontinuities, from the microwave point of view it is quite complex due to the mixture of air and water. This mixture has a high impact on the mapped height. Indeed, the wave propagates into the snow/ice to a depth that depends on the material property. The measured height, i.e. the measured scattering phase center, depends on this property and in particular on the complex dielectric constant  $\epsilon_r = \epsilon_r' - j\epsilon_r''$ .

With more detail, the wave propagates as an electromagnetic field (Richards, 2009):

$$E(r) = E_0 \exp(-\Gamma r) = E_0 \exp(-\alpha_a r - j\beta r), \quad (1)$$

where  $E_0$  is the magnitude of the field,  $r$  is the wave direction and  $\Gamma = \alpha_a + j\beta$  is the *complex propagation constant*, whose real part  $\alpha_a$  describes the field losses caused by the medium. It is also called *attenuation constant* and can be approximated as:

$$\alpha_a = \frac{\pi}{\lambda} \frac{\epsilon_r''}{\sqrt{\epsilon_r'}}, \quad (2)$$

where  $\lambda$  is the wavelength. The approximation is valid when  $\epsilon_r'' < \epsilon_r'$ . Thus,  $\epsilon_r$  is the key parameter here, as it describes the medium properties in relationship to the electric field, i.e. how its power decreases in the medium through which it travels. The loss of power density is described by the *penetration depth*:

$$\delta = \frac{\lambda}{2\pi} \frac{\sqrt{\epsilon_r'}}{\epsilon_r''}, \quad (3)$$

i.e. the value of  $r$  for which its power is reduced to 1/e. Deeper penetration is measured for low bandwidths and low moisture contents ( $\epsilon_r''$  is proportional to moisture).

$\delta$  approximates the measured elevation from the radar system:

$$\hat{h} = h_{sup} - \delta \cos(\theta), \quad (4)$$

where  $h_{sup}$  is the terrain elevation and  $\theta$  is the look angle.

A more in-depth description about the radio wave propagation can be found in several dedicated books, e.g. Ishimaru (1978). A discussion of the microwave theory relevant to the present study is given in the following sections.

### 2.1. Dielectric constants of frozen environments

The penetration of the radar wave into ice and snow is a well-studied topic. Empirical results in Rignot, Echelmeyer, and Krabill (2001) showed small penetration over exposed ice (1–2 m in C-band) and large penetration (up to 10 m in C-band) for dry firn. In the following analysis, the penetration depth is quantified employing the models of Hallikainen, Ulaby, and Abdelrazik (1986) for dry and wet snow. Although the temperate Vatnajökull glacier has no dry snow facies (Williams, Hall, & Benson, 1991), their dielectric modelling is

provided for completeness. This analysis serves to trace a line regarding the absolute height accuracy of TanDEM-X DEMs and the radar altimeter used for comparison in Section 6. The system bandwidth of these two systems is different: while altimeter works in C-band, TanDEM-X data are acquired in X-band.

### 2.2. Dry snow

Dry snow consists of ice crystals and air. The parameter triggering the dielectric constant, hence the penetration depth, is the snow density. To provide an example, powder snow has a density of about 0.05 g/cm<sup>3</sup> whereas an extremely dense old snowpack has a density of about 0.5 g/cm<sup>3</sup> (Cuffey & Paterson, 2010). To quantify the penetration depth, the model of Hallikainen et al. (1986), valid for densities below 0.5 g/cm<sup>3</sup>, is considered:

$$\begin{aligned} \epsilon_{ds}' &= 1 + 1.9\rho_{ds} \\ \epsilon_{ds}'' &= \frac{0.34V_i\epsilon_i''}{(1 - 0.417V_i)^2} \\ V_i &= \frac{\rho_{ds}}{0.916}, \end{aligned} \quad (5)$$

where  $\rho_{ds}$  is the dry snow density,  $V_i$  the volume fraction of ice in the mixture and  $\epsilon_i$  is the ice dielectric constant. The depth for three different densities is given in Table 1.

### 2.3. Wet snow

Wet snow adds liquid water volume  $V_w$  [% vol] to the dry snow composition. A useful model for computation is the following (Hallikainen et al., 1986):

$$\begin{aligned} A &= 1.0 + 1.83\rho_{ds} + 0.02V_w^{1.015} \\ B &= C = 0.073 \\ f_0 &= 9.07 \\ \epsilon_{ws}' &= A + \frac{BV_w^{1.31}}{1 + (f/f_0)^2} \\ \epsilon_{ws}'' &= \frac{C(f/f_0)V_w^{1.31}}{1 + (f/f_0)^2}. \end{aligned} \quad (6)$$

The penetration depth for three different water volume contents and a fixed snow density of 0.3 g/cm<sup>3</sup> is given in Table 1. The wave penetration dependency on the water content is depicted in Fig. 2 for the two systems under study. According to the International Classification for Seasonal Snow on the Ground (ICSSG) (Fierz et al., 2009), the water content x-axis in Fig. 2 is classified in three areas. Snow is *moist* when the water is not visible even at 10× magnification. *Wet* snow implies water visibility at 10× magnification, but water cannot be pressed out by squeezing snow. Instead, this is possible for *very wet* snow. The SAR wave penetration depth for the last two categories is limited to a few decimeters. In contrast, for very low levels of moisture, the penetration depth can also reach few meters. The snow density has a little impact in

**Table 1**

Penetration depth in dry and wet snow for TanDEM-X and the radar altimeter employed for validation. Dry snow penetration depth is computed for three different snow densities, representing newly fallen snow ( $\rho_{ds} = 0.1$ ), dense snowpack ( $\rho_{ds} = 0.3$ ) and extremely dense old snowpack ( $\rho_{ds} = 0.5$ ). Wet snow penetration depth is computed at three different water contents and fixed snow density of 0.3 g/cm<sup>3</sup>.  $\Delta h_{Alt-TDX}$  represents the difference between the altimeter and the TanDEM-X depths.

Snow type	Property	TanDEM-X [m]	Altimeter [m]	$\Delta h_{Alt-TDX}$ [m]
dry snow	$\rho_{ds} = 0.1$	69.4	208.8	145.4
	$\rho_{ds} = 0.3$	21.8	65.4	43.6
	$\rho_{ds} = 0.5$	11.6	35.0	23.4
wet snow	$V_w = 1$	0.17	0.5	0.33
	$V_w = 2$	0.07	0.21	0.14
	$V_w = 3$	0.04	0.12	0.08

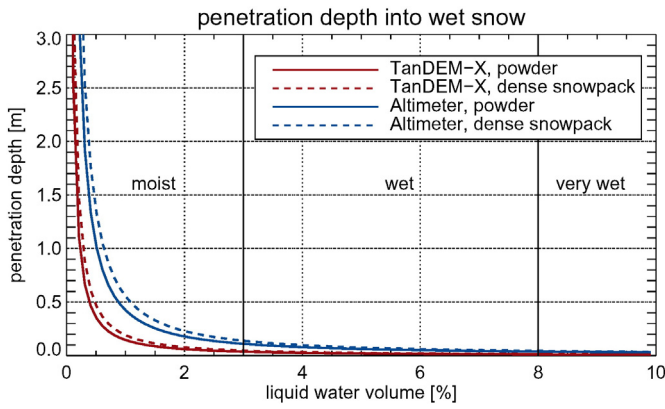


**Fig. 2.** Penetration depth in wet snow terrain type for TanDEM-X and the radar altimeter employed for validation. Two extreme snow densities are plotted for each system: newly fallen powder snow ( $\rho_{ds}=0.05$ ) and extremely dense old snowpack ( $\rho_{ds}=0.5$ ). Intermediate densities lie in between the two curves. Snow wetness is classified according to the *International Classification for Seasonal Snow on the Ground* in three categories: moist, wet and very wet.

the penetration depth for wet snow cover. To be noticed, the *wet* classification tag of the ICSSG can create some confusion since it overlaps with the more general *wet snow* dielectric classification name. The dielectric classification, as shown in Table 1, simply differentiates the snow in presence of liquid water volume (*wet snow*) and without it ( $V_w = 0$ , *dry snow*).

This analysis is relevant for the application presented in this paper since the Vatnajökull glacier can be considered of wet snow dielectric type with variable liquid water volume (Williams et al., 1991). Overall, the elevation discrepancy between TanDEM-X and altimeter is expected to be below one meter, assuming the same snow conditions and a liquid water volume higher than 0.5 [%<sup>vol</sup>].

#### 2.4. Generalization to temporal InSAR DEMs

A temporal DEM series analysis is often used for scientific purposes to analyze topographical changes (Albino et al., 2015; Kubanek et al., 2015; Poland, 2014; Rott et al., 2014). A relevant issue, which occurs in temporal studies, is the relative calibration of the DEMs. Indeed, differently calibrated DEMs result in the misinterpretation of the obtained results. For glacial environments, the calibration can be a huge processing problem, since the terrain elevation is continuously changing depending on the local Earth dynamics. A reasonable approach consists in the DEM calibration using external references, as explained in Section 4.

According to the equations in the previous section, the parameters affecting the final elevations are the physical snow properties, the sensor looking angle and sensor frequency.

Physical snow properties strongly influence the final elevation value. As shown in Table 1, the phase center variations can be very high (up to tens of meters) due to different parameters, such as the water content and the snow type. Thus, if the purpose is to track dynamical changes, the data stack should be characterized by the same snow properties. This is a very stringent constraint but should definitively be taken into account in the analysis.

System wavelength enters in all the snow relative permittivity models. Larger wavelengths yield larger penetrations. Fig. 3 shows the height discrepancy between a TanDEM-X DEM and another DEM acquired at a different frequency. In the figure, for completeness, also the elevation discrepancy over pure water ice at two temperatures is represented according to the Mätzler and Wegmüller (1987) permittivity model. Additionally, the C-band SRTM (Rabus, Eineder, Roth, & Bamler, 2003) and Tandem-L (Krieger et al., 2009) operating frequencies are highlighted.

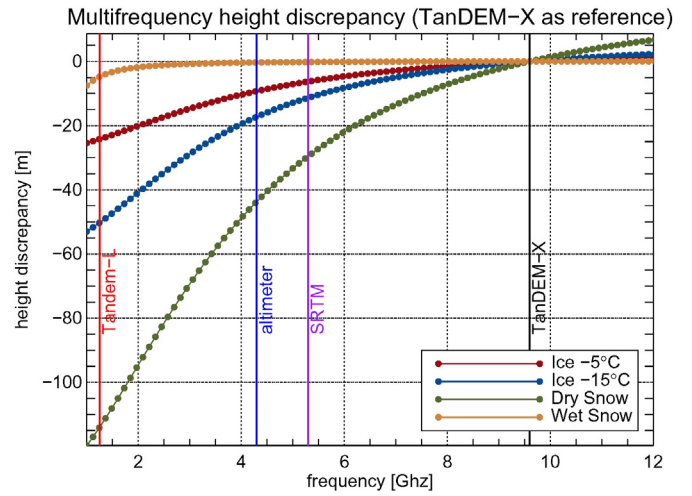


**Fig. 3.** Height discrepancy between a TanDEM-X DEM and another DEM acquired at a different frequency. In the x-axis, the frequency is spanning from L-band to X-band. Four different terrain types are considered; dry snow is assumed with a fixed density of 0.3 g/cm<sup>3</sup> and wet snow is assumed with the same density and a volumetric water content of 1 [%<sup>vol</sup>].

The other system parameter impacting on the scattering phase center, as a weight to the penetration depth, is the radar look angle. Limit cases are flat look angle (90 deg), yielding no penetration, and vertical look angle (0 deg), bringing maximum penetration. Radar scenes acquired at different look angles thus yield different elevations.

A temporal analysis of frozen environment with InSAR DEMs is very sensitive to the system parameters and to the snow status. The comparison of DEMs over specific areas should be performed in the same time of year (and even the same hour) to ensure similar snow dielectric properties. Moreover, the same weather conditions should also be assured. Additionally, it makes no sense to use DEMs acquired at different bands without their re-calibration for the different penetrations.

### 3. System parameters impact on DEM uncertainty

System parameters have a strong influence on DEM accuracy. In contrast with Section 2, this section deals with the phase error related to decorrelation and SAR geometry, impacting on the relative elevation accuracy. In InSAR processors, random error is measured with the coherence parameter. Coherence assesses the quantity of decorrelation which occurs between the two SAR signals. It is defined as the cross-correlation between the two complex SAR images  $x_1$  and  $x_2$  and can be estimated as:

$$\gamma = \frac{\left| \sum x_1 x_2^* \exp\{-j\phi_{\text{known}}\} \right|}{\sqrt{\sum |x_1|^2 \sum |x_2|^2}} \quad (7)$$

In Eq. (7),  $\phi_{\text{known}}$  is a deterministic phase value representing the topography and other known phase trends in the estimation window. This factor must be compensated to accomplish stationarity (Touzi, Lopes, Bruniquel, & Vachon, 1999). Given the coherence, the marginal probability density function for the interferometric phase  $\phi$  is derived using *gamma*  $\Gamma$  and *hypergeometric F* functions (Just & Bamler, 1994):

$$p(\phi; \gamma, L) = \frac{\Gamma(L + 1/2)(1 - \gamma^2)^L |\gamma| \cos(\phi - \phi_0)}{2\sqrt{\pi}\Gamma(L)(1 - \gamma^2 \cos^2(\phi - \phi_0))^{L+1/2}} + \frac{(1 - \gamma^2)^L}{2\pi} {}_2F_1\left(L, 1; \frac{1}{2}; \phi^2 \cos^2(\phi - \phi_0)\right), \quad (8)$$

where  $L$  is the independent number of looks and  $\phi_0$  is the coherence argument. The standard deviation of the interferometric phase  $\sigma_\phi(x, y)$  is derived by integrating Eq. (8). The DEM standard error for every range and azimuth samples  $(r, a)$  is calculated as:

$$h_{err}(r, a) = \sigma_\phi(r, a) \frac{h_a}{2\pi}, \quad (9)$$

where  $h_a$  is the height of ambiguity, i.e. the height difference generating an interferometric phase change of  $2\pi$ . The DEM standard error depends then on the coherence and it is scaled by the height of ambiguity. Higher heights of ambiguity yield higher errors. There is actually a limit for the height of ambiguity, since lower ambiguities yield low standard errors, but the unwrapping stage may be very complex, producing errors well above the theoretical standard ones.

Coherence loss can be decomposed into several factors (Zebker & Villasenor, 1992). Neglecting the temporal, the volume and the system decorrelations, we focus here just on the topographical impact of the mapped scene into the generated DEM, due to the mountainous environment under study. For that, the spectral shift theory shall be introduced. The basic concept is that the range spectra of a SAR image is varying depending on the look angle. A look angle discrepancy, as in the InSAR case, yields a shift in the range spectra, measured as (Gatelli et al., 1994):

$$\Delta f = \frac{f}{\tan(\theta - \alpha)} \Delta\theta, \quad (10)$$

where  $\theta$  is the master look angle,  $\alpha$  the terrain slope and  $\Delta\theta$  the look angle difference between slave and master channels. Eq. (10) can be rewritten with system parameters:

$$\Delta f = \frac{cB_\perp}{\lambda R \tan(\theta - \alpha)}, \quad (11)$$

where the speed of light  $c$ , the perpendicular baseline  $B_\perp$  and the master reference range  $R$  are introduced. The shift produces spatial decorrelation:

$$\gamma_{spatial} = 1 - \left| \frac{\Delta f}{B_w} \right|, \quad (12)$$

where  $B_w$  represents the system bandwidth. This decorrelation can be then expressed as height error by computing the standard deviation of the interferometric phase according to  $\gamma_{spatial}$  in Eq. (8) and solving for Eq. (9). In the next section, the theoretical considerations described in Section 2 and in this section are applied to the current dataset.

#### 4. TanDEM-X dataset

The TanDEM-X dataset used for this study is composed of five bistatic acquisitions covering the Bárðarbunga caldera and the northwestern part of the Vatnajökull glacier. The main system parameters are given in Table 2. The height of ambiguity is high enough to ensure a phase unwrapping without errors.

##### 4.1. DEM accuracy

The absolute TanDEM-X height error with respect to the superficial ice cap height can be estimated given a ground truth. This was not available due to the ongoing hazard, but several profiles taken with a radar altimeter were available and are analyzed in Section 6. Nevertheless, for the caldera subsidence monitoring, a constant absolute error over the stack is tolerated since the interest is on the relative height differences. Thus, it is important to ensure a consistent phase center location for all data in the stack. According to the electromagnetic considerations in Section 2, uniform snow conditions and a constant

**Table 2**

Geometrical and quality parameters of the TanDEM-X test site under study.  $B_\perp$ ,  $h_a$ ,  $\theta$ ,  $\bar{\gamma}$ ,  $\overline{h_{err}}$  and  $q_{ratio}$  represent the perpendicular baseline, the height of ambiguity, the incidence angle of center scene, the mean coherence of the entire scene, the mean standard height error of the entire scene and the quality ratio, respectively.

Acquisition date	$B_\perp$ [m]	$h_a$ [m]	$\theta$ [deg]	$\bar{\gamma}$	$\overline{h_{err}}$ [m]	$q_{ratio}$
01.08.2014	29.7	163.3	31.4	0.86	2.3	99.9
12.08.2014	31.1	156.2	31.4	0.80	2.8	99.9
17.10.2014	50.2	96.6	31.4	0.92	0.94	99.9
28.10.2014	38.2	126.8	31.4	0.92	1.2	99.9
08.11.2014	57.8	84.2	31.4	0.91	0.89	100.0

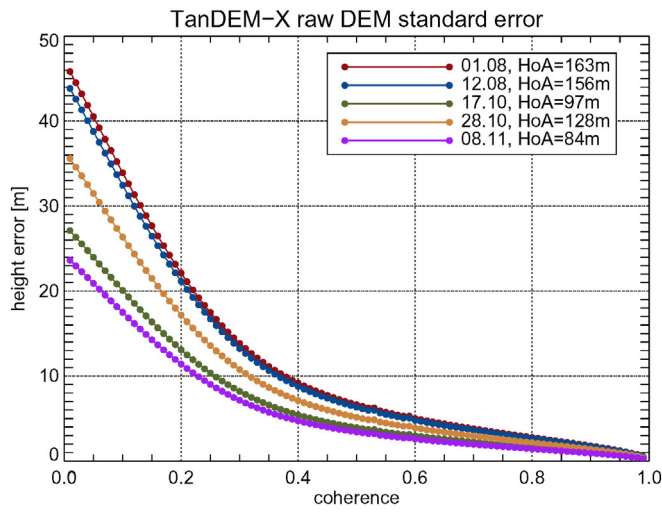
incidence angle are required. While the stack incidence angle is not varying, a uniform snow condition is more difficult to assess, since different periods of the year may have a strong impact. However, the high elevation of the caldera, about 2000 m above sea level, the constant SAR early acquisition time, 07:49 a.m., and the consequent low temperature, always below zero degrees Celsius, prevent melting issues. Assuming then the absence of freshwater ice, the discussion should move to the wetness of the snow at the moment of the acquisition. This investigation is performed in Section 5 through a temporal backscatter analysis.

Regarding the system impact on the relative height accuracy, the variation of the height error depending on the local coherence, as in Eq. (9), is depicted in Fig. 4(a). The system heights of ambiguity yield errors below 2 m for coherence values below 0.9. A total of 35 looks are used in the processing (7 in range and 5 in azimuth), resulting in an independent number of looks of about 25 (Krieger et al., 2007). Fig. 5(a) shows the height error computed with the local coherence for the October 17, 2014, acquisition. Height errors are strongly correlated with terrain slope, represented in Fig. 5(b). The theoretical height error dependency with terrain slope is depicted in Fig. 4(b) for the five acquisitions under study. These curves do not apply for shadow and layover areas, where the measured elevation is not reliable (Deo, Rossi, Eineder, Fritz, & Rao, 2015; Rossi & Eineder, 2015); the two regions are marked in the plot. Layover is defined for slopes which are larger than the system looking angle and corresponds to regions where multiple terrain portions are mapped in a single resolution cell. Shadow is defined for slopes which are smaller than the complementary of the system looking angle and represents regions which are not seen by the radar. Slopes are not expressed in absolute values since they are considered in the SAR range direction: positive slopes are the ones facing the radar, while negative slopes are the ones tilted away. The height error tends toward infinite values at slopes close to the looking angle, whereas it goes toward zero at tilted slopes close to the shadow boundary. The flat slopes of the Bárðarbunga caldera yield errors of about 10–20 cm for the TanDEM-X InSAR configuration under analysis.

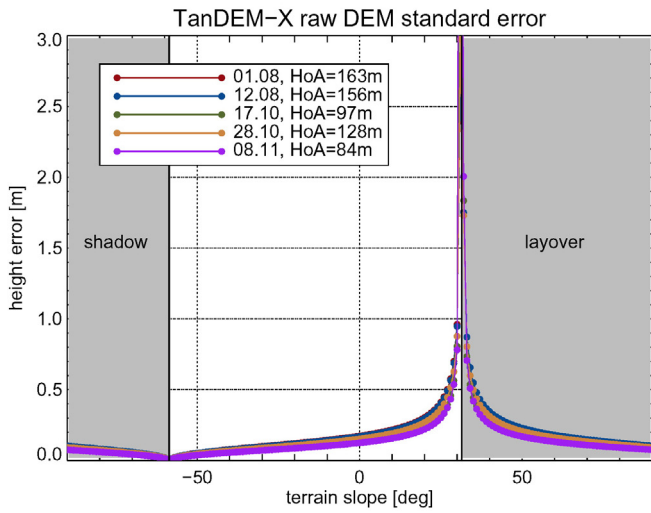
The mean quality parameters over the entire scenes are given in Table 2. The mean coherence  $\bar{\gamma}$  is very high for all acquisitions, yielding low height errors  $\overline{h_{err}}$ . The quality ratio  $q_{ratio}$  indicates the percentage of the scene which is not affected by unwrapping errors (Rossi, Gonzalez, Fritz, Yague-Martinez, & Eineder, 2012), revealing the absence of unwrapping errors for all DEMs. It should be noted that the mean height error specified in the table is not absolute, i.e. the height discrepancy between the top of the glacier and the phase center is not accounted for.

##### 4.2. In-processing calibration

DEM calibration is probably the most important processing step of any multi-temporal elevation study, since uncalibrated data provide misinterpretations of the geophysical outcomes. The calibration can be performed as an in-processing or as a post-processing step; both of these techniques require a reference elevation model or ground control points. An in-processing calibration has been proposed in Rossi et al., 2012. The elevation reference is in this case the coarse but absolute



(a) height error vs coherence

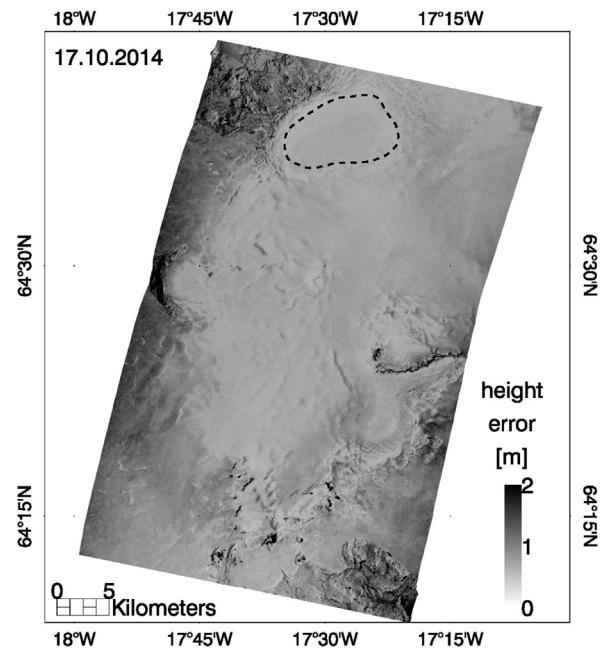


(b) height error vs terrain slope

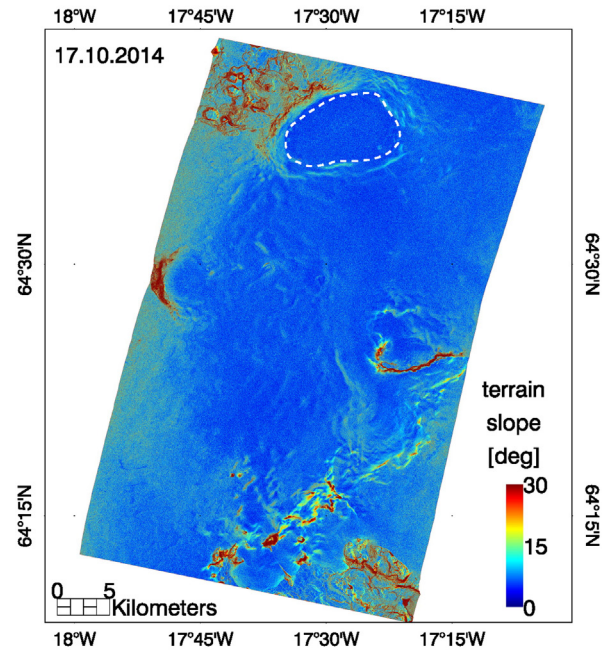
**Fig. 4.** Standard height error trends of the five acquisitions under study. (a) Error dependency with the local coherence. (b) Error dependency with terrain slope. Shadow and layover areas do not provide accurate results and the corresponding marked curves are therefore not applicable. Slopes are measured in range direction: positive slopes are the ones facing the radar, while negative slopes are the ones tilted away.

DEM generated by transforming the radargrammetric coregistration shifts into an elevation model. This method is used in the Integrated TanDEM-X Processor (ITP) to internally calibrate the DEM by estimating the absolute phase offset.

Although the method in Rossi et al., 2012 is a feasible solution for a single DEM calibration, it should be applied with precaution for a temporal stack of DEMs over the same area. This is because every single absolute phase offset estimation is independent and based on the local InSAR geometry, and baseline inaccuracies may vary between geometries, thus producing absolute height differences between DEMs. For this reason, the calibration using a common reference is a more favorable solution. If the purpose is to check topographical changes relative to one of the acquisitions in the data stack, then the quality of the reference is not important and a simple ellipsoidal model at a certain height can be employed. However, if DEMs acquired with different techniques are employed, then a reliable source should be taken for calibration, such as SRTM or TanDEM-X DEMs. Since complementary



(a) height error map



(b) terrain slope map

**Fig. 5.** (a) Height error map for the October 17, 2014, take computed with the local coherence. (b) Terrain slope computed from the same take. The Bárðarbunga caldera outline is highlighted.

altimetric data are used for validation, an accurate source must be exploited for the TanDEM-X stack analyzed in the paper.

To calibrate the data stack, the operationally mosaicked TanDEM-X DEM has been employed (Gruber, Wessel, Huber, & Roth, 2012). A single DEM tile is spanning 1 square degree with a sampling of 12 m. The employed tile is highlighted in Fig. 1. This elevation model can be taken as precise ground truth over land portions but

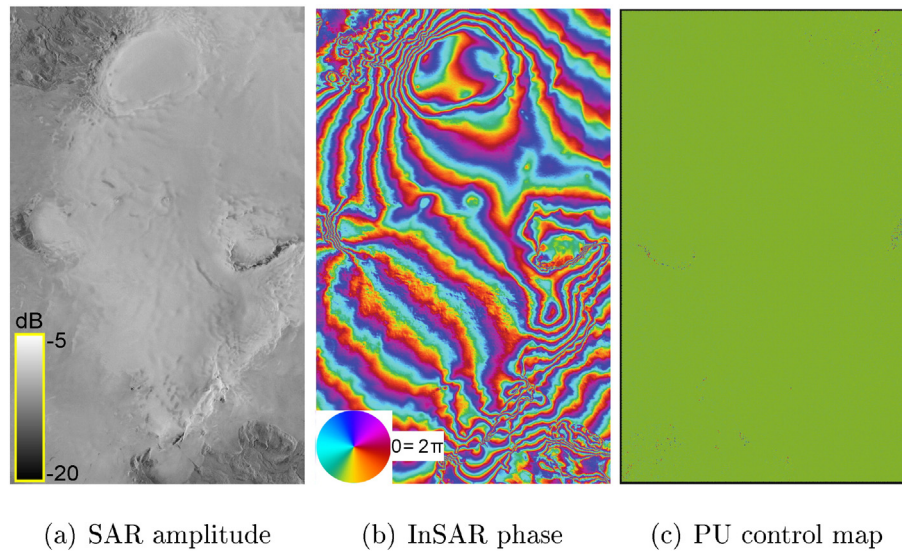


Fig. 6. Master channel calibrated amplitude (a), interferometric phase (b) and phase unwrapping control map (c) of the TanDEM-X acquisition on 08.11.2014.

it should be taken with care over glacier surface (considering the analysis in Section 2.2). Indeed, 25 separate acquisitions spanning three years (2011–2014) have been mosaicked to produce this DEM. Different seasons, yielding different scattering centers, may have been combined depending on the local coherence (Gruber et al., 2015). The resulting scattering center is then unknown and may not fit with some temporal data. For this reason, this DEM should not be used as absolute reference for the sole Bárðarbunga caldera. Nevertheless, the single TanDEM-X scene is quite large ( $30 \times 50$  km), and includes land portions, which exclusively have been used in the computation of the absolute phase offset. In summary, this offset is a single value computed by transforming the reference DEM in interferometric phase, which is then compared with the unwrapped phase generated during processing. The offset is added to the unwrapped phase for the generation of a DEM which is consistent with the reference. Phase unwrapping is not an issue here. Fringes are well separated even at steep topography (Fig. 6(b)) and the control map (Rossi et al., 2012) reveals no unwrapping errors (Fig. 6(c)).

## 5. Temporal analysis

To evaluate the topographical changes, the DEMs are generated over a prearranged geographical grid with a spacing of about 6 m in latitude and longitude. The interferogram horizontal resolution, computed taking into account the independent number of looks and the SAR cell resolution, is about 9 m.

The DEM differences between the first DEM in the stack (August 01, 2014) and all the others are displayed in Fig. 7. The Bárðarbunga caldera contour is traced according to the outline sketched in Sigmundsson et al. (2015). Fig. 7(a) shows the differential height on August 12, 2014. Here, no relevant changes are noticeable since this topographical map represents the elevation differences with a reference time lag of just 11 days and still before the main fissure opened up in the Holuhraun plain. The small-scale topographical changes are mainly due to system noise. Instead, the topographical maps in Fig. 7(b), (c) and (d) are relevant since respectively showing the topographical changes 47, 58 and 69 days after the main eruption started. The most prominent topographical change is the caldera subsidence, originated by the collapse of part of the ground above the magma chamber. The considerable depression left in the landscape, with subsidence peaks above 50 m for the largest time lag in Fig. 7(d), is quite visible. The formation of icecap cauldrons at the south-eastern rim of the caldera is also noticeable. Moreover, these differential maps reveal the complete topographical

changes over the northwestern portion of the Vatnajökull glacier. Among them, two accumulations at the eastern Skaftá cauldron and at the Grímsötn volcanic system are conspicuous, considered to result from uplift of the glacier surface due to water accumulation in these well-known geothermal areas (e.g. Björnsson, 2003). They are annotated in Fig. 7(b).

The result of a quantitative study on the caldera subsidence is displayed in Table 3. SAR backscatter is measured by calibrating the amplitude signal and compensating for the local incidence angle. The reference DEM shown in Fig. 1 has been used for the computation of the local incidence angle. The mean caldera backscatter is given in the second column of Table 3. Summer acquisitions exhibit a low backscatter, about  $-15$  dB, whereas autumn acquisitions exhibit a higher one, about  $-9$  dB. The work of Stiles and Ulaby (1980) helps to clarify the relationship between backscatter and snow properties. First of all, the backscattering coefficient decreases with snow wetness. According to the analysis in Stiles and Ulaby (1980), the measured summer backscatter corresponds to a liquid water volume larger than 1 [%<sup>vol</sup>], making the TanDEM-X height estimate very close to the surface top (see Fig. 2). In contrary, autumn acquisitions exhibit a backscatter which yields a lower liquid water volume, therefore prone to a larger penetration into snow. An empirical analysis over the large glacier area at the south-east of the caldera, chosen in order to avoid evident topographical changes and marked in Fig. 7(d), reveals a mean difference of 1.26 m. This difference, according to Fig. 2, corresponds to a liquid water content for the autumn acquisitions which is smaller than 0.5 [%<sup>vol</sup>].

The mean coherence over the caldera given in the third column is in general very high and the relative height error in the fourth column is respectively low.

The caldera collapse is evaluated in terms of mean height and volume changes in the fifth and sixth column of Table 3, respectively. These mean values represent the average change over the caldera outline depicted in Fig. 7. For the last stack acquisition, thus 84 days after the onset of the volcanic unrest and 69 days after the main fissure opening, the caldera already sunk in average by 16 m, with peaks of about 50 m in its north-eastern part (see next section), and with an impressive volume loss of about 1 billion cubic meters. This yields an average rate of change over the caldera of about one meter per week.

For subglacial volcanoes such as Bárðarbunga, the caldera subsidence does not refer just to the ground volume loss related to the eruption, but also to the melting of snow/ice because of heating flux release from the magma intrusion. A peculiar aspect of this eruption is

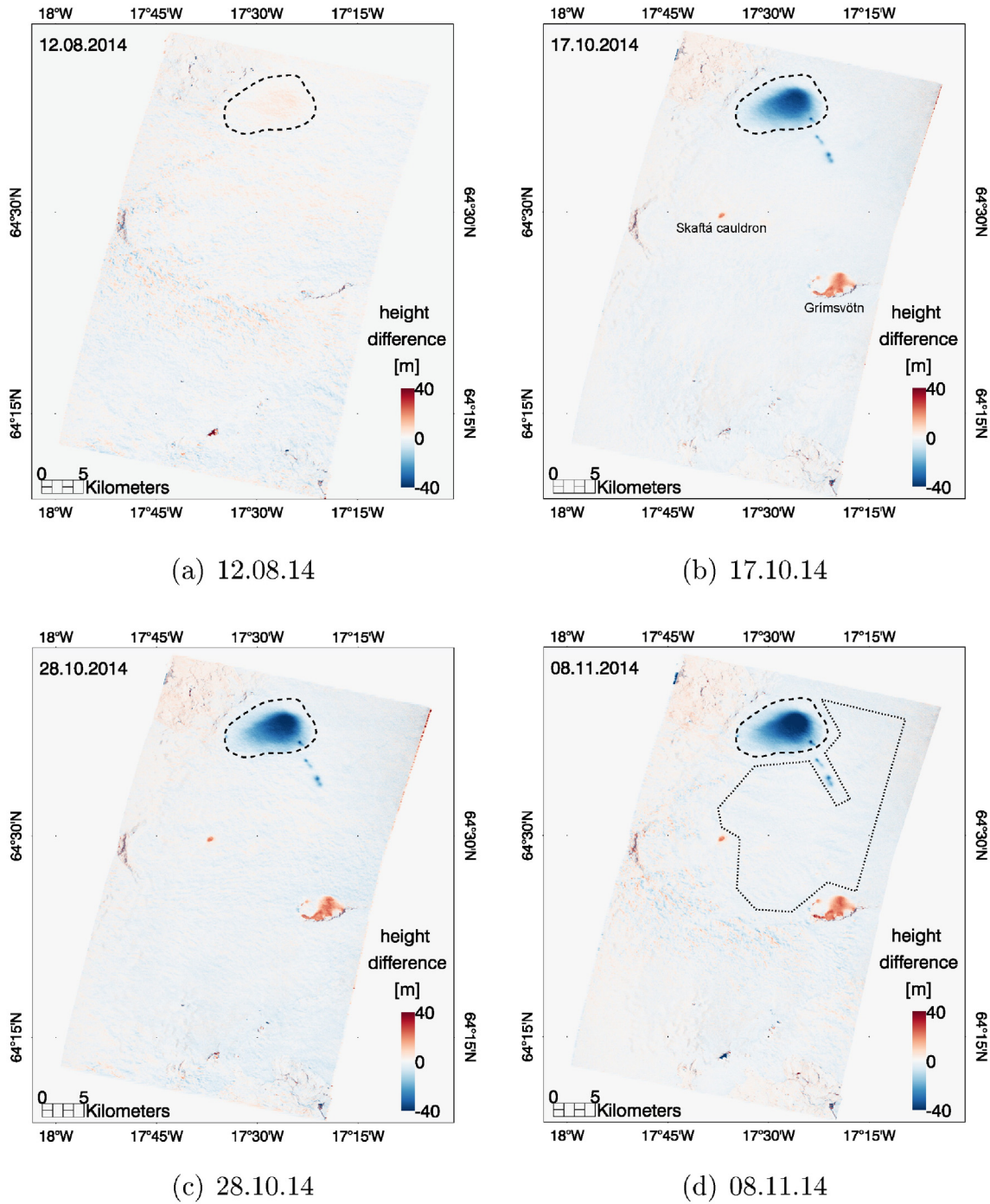


Fig. 7. DEM differences relative to the first DEM in the stack (01.08.2014). Bárðarbunga caldera is highlighted in all the differences. The dashed area at the south-east of the caldera in (d) is the one used to evaluate the seasonal wave penetration difference.

Table 3

Mean value of relevant parameters computed over the Bárðarbunga caldera. The six columns represent, from left to right, acquisition date, mean calibrated SAR backscatter of the master acquisition, mean coherence, mean standard height error, mean DEM difference between first stack acquisition and current data, mean volume difference between first stack acquisition and current data.

Acquisition date	$\sigma_0$ [dB]	$\gamma$	$h_{err}$ [m]	$\Delta \bar{h}_{1.8}$ [m]	$\Delta V_{1.8}$ [m <sup>3</sup> ]
01.08.2014	$-15.23 \pm 0.86$	$0.90 \pm 0.03$	1.34	-	-
12.08.2014	$-15.31 \pm 0.75$	$0.90 \pm 0.03$	1.70	0.52	0.33e8
17.10.2014	$-9.86 \pm 0.74$	$0.96 \pm 0.01$	0.63	-13.85	-8.81e8
28.10.2014	$-9.75 \pm 0.76$	$0.96 \pm 0.01$	0.55	-15.13	-9.62e8
08.11.2014	$-9.60 \pm 0.77$	$0.94 \pm 0.01$	0.69	-16.39	-10.4e8
Reference	-	-	0.67	-4.53	-2.88e8

that jökulhlaups related to the cauldrons formation at the caldera rim, the south-east flank of the Bárðarbunga, or above the dike intrusion north-west of Bárðarbunga, where minor subglacial eruptions probably occurred, were never observed. The water location release is still unknown, and possibly most of it is drained into the groundwater system below the Vatnajökull glacier (Magnússon, 2015). A one-to-one comparison of the derived volume loss, for validation purposes, with external lava volume measurements is therefore not possible since one of the volume sources remains unknown. Nevertheless, it is meaningful to compare our caldera volume loss estimation, 1.08 km<sup>3</sup>, with the lava volume extent measured on November 04, 2014 (Institute of Earth Science, 2014),  $1.0 \pm 0.3$  km<sup>3</sup>, thus 4 days before our estimate.

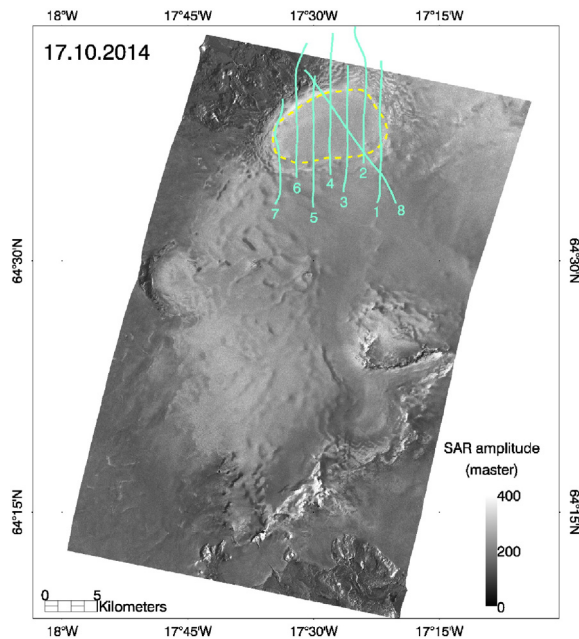


Fig. 8. Altimeter tracks used for height profiling over the Bárðarbunga caldera.

Considering the seasonal discrepancy of the phase scattering center, our caldera loss estimate is corrected to a volume of  $0.963 \text{ km}^3$ . The two estimates are very similar, although the caldera loss originated by the additional loss contribution created by the ice melting is not compensated. It should be noted that a consistent role in the volume comparison can arise from the newly formed cauldrons, which are not considered in the caldera volume loss and whose subsidence may be associated to the lava volume. Other phenomena, such as glacial eruptions and dyke widening, may also impact in the comparison, since they affect the lava volume measure. In general, a ratio of one between the erupted volume and the subsidence volume indicates that the crust deformation is fully compensated by the compressibility of the magma (Johnson, Sigmondsson, & Delaney, 2000).

## 6. Profile analysis

An extensive campaign has been performed by the University of Iceland over the Bárðarbunga caldera and its surroundings. It consisted of several flights on 16 days between September 09, 2014, and April 10, 2015, with an aircraft carrying a radar altimeter, that measures every 15–20 m the height with an absolute accuracy of 2–3 m (Guðmundsson et al., 2007). The altimeter operates in C-band at a frequency of 4.3 Ghz. Eight profiles acquired over the caldera on October 24, 2014, are displayed in Fig. 8. Among them, tracks 1, 3, 7 and 8 are analyzed in detail in the following paragraphs.

**Track 1.** The first profile covers the eastern portion of the caldera and one of the new cauldrons located at the intersection with Track 8. The top-left plot in Fig. 9 shows the absolute heights of all temporal measurements. To better evaluate the topographical changes, the center-left plot displays the differences with the first data in the stack. Here, the greater temporal change occurs over the cauldron, with an elevation loss of about 15 m (an average rate of 15 cm/day measured between October 17 and November 08), whereas the external part of the caldera included in the profile shows a loss of about 5 m. Radar altimeter elevations are matching with TanDEM-X measurements, excluding the beginning and final portion of the profile, outside the caldera. To better evaluate the discrepancies between TanDEM-X and radar altimeter, the TanDEM-X elevation data have been interpolated to match the exact time and date of the altimeter acquisitions. The result is displayed at the bottom-left of Fig. 9. In principle, the different scattering center yields an elevation difference among them (Eq. 3). With the same snow conditions, the C-band altimeter elevation is lower than the X-band TanDEM-X one (Section 2, Fig. 2). Here, one notices a lower scattering center for the altimeter of 3–5 m in the proximity of the caldera, and a lower scattering center of TanDEM-X data of about one meter in the caldera position. The reason for this trend is the non-linearity of the phase center in the course of the day (Stiles & Ulaby, 1980). Indeed, all the TanDEM-X acquisitions were gathered at 07:49 a.m., in the early morning. At midday, it is reasonable to assume that the snow water content is higher than early in the morning, due to the increasing temperature, thus causing a higher phase center, even very close to the surface top. However, it is interesting to notice that outside the caldera, the altimeter measures a lower height. Different snow dielectric properties are a possible explanation for this.

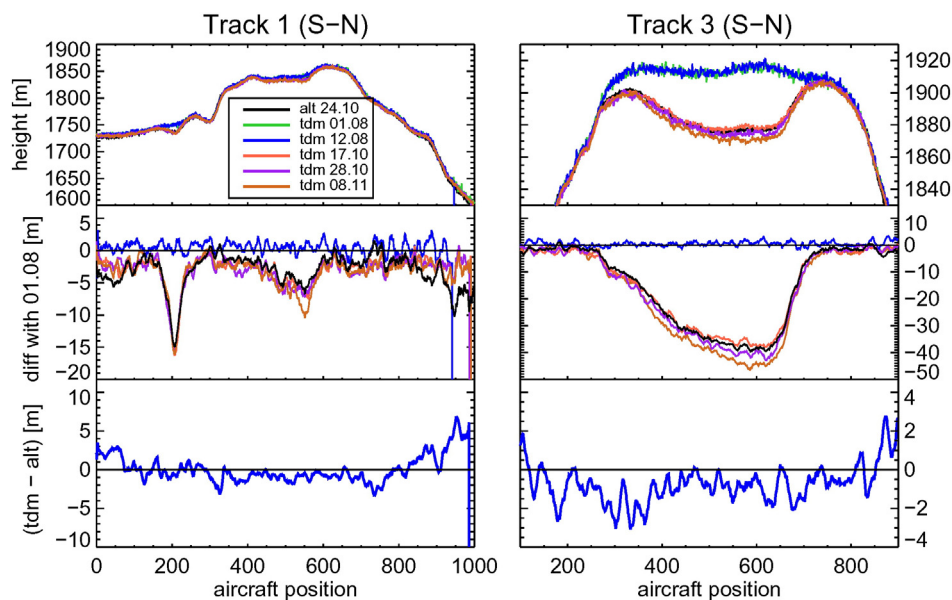
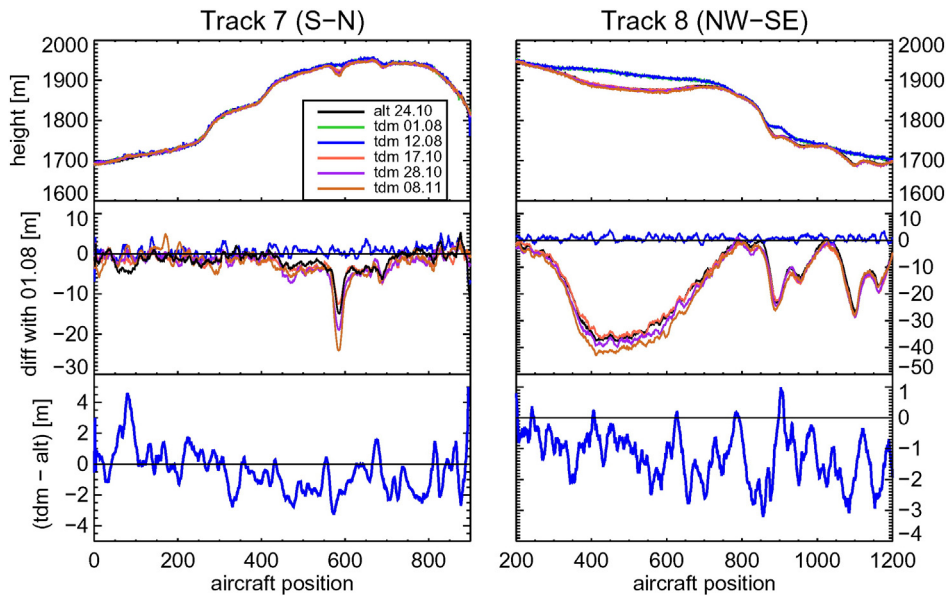


Fig. 9. (left) Elevation measured for the five TanDEM-X acquisitions and the altimeter over Track 1 (top-left), elevation differences with the first data in the stack (center-left) and elevation difference between altimeter and TanDEM-X data interpolated at the date and time of the altimeter acquisition. (right) Same plot structure but for Track 3.



**Fig. 10.** (left) Elevation measured for the five TanDEM-X acquisitions and the altimeter over Track 7 (top-left), elevation differences with the first data in the stack (center-left) and elevation difference between altimeter and TanDEM-X data interpolated at the date and time of the altimeter acquisition. (right) Same plot structure but for Track 8.

*Track 3.* Profile 3 intersects the highest change in the caldera, with changes of more than 40 m (right side of Fig. 9). The maximum rate of subsidence at this location is 49 cm/day, in accordance with the measurement of Riel et al. (2015), who reported a rate of 50 cm/day. The caldera structure is not symmetric, and its lowest depression lies at its north-east part. Morning phase center at X-band is always lower than midday phase center at C-band, as shown in the bottom-right plot of Fig. 9.

*Track 7.* Profile 7 covers the western rim of the caldera and reveals a small cauldron at around aircraft position 600, as visible in the center-left plot of Fig. 10. The elevation difference at the cauldron location between October 17 and November 08 is with 13 m rather high,

corresponding to a subsidence rate of about 60 cm/day. The phase center difference at the caldera position is approximately one meter.

*Track 8.* Track 8 runs diagonally through the caldera and intersects two cauldrons at the south-eastern rim. The Bárðarbunga caldera reaches 40 m of subsidence with a maximum subsidence rate of 36 cm/day. The mass loss for the south-eastern cauldrons is smaller, approximately 30 m at maximum. They exhibit a double minima structure, visible also from the differential maps in Fig. 7. Their maximum subsidence rate, equal to 18 cm/day, is about half of the caldera's rate for this track.

*Discussion.* The analysis of the profiles increases the understanding of the penetration depth of the X-band signal in the caldera during the

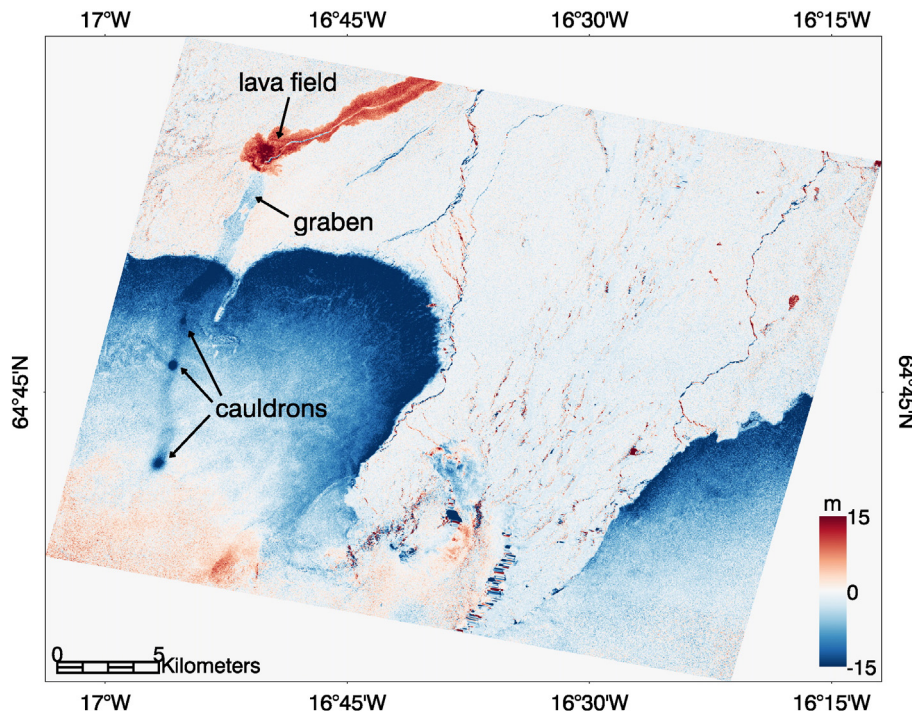


**Fig. 11.** Graben structure and lava flow revealed by differentiating a post-event TanDEM-X raw DEM (09.09.14) and a pre-event DEM (11.11.11).

volcanic activity. The combined analysis in Figs. 9–10 reveals a discrepancy of up to 2 m between TanDEM-X and altimeter data. Considering that the altimeter is also an active system and thus subjected to wave propagation issues, it is not possible to draw a self-assured evaluation of the penetration depth, and, for instance, invert the models in Eq. (5) to derive snow properties. Nevertheless, it has been shown how the X-band signal during the morning has a lower extinction than C-band signal at midday. In other words, the changes of snow wetness strongly impact on the phase centers and the result interpretations. Results provided by TanDEM-X overestimate – though very slightly – the subsidence rate of the caldera. Nonetheless, the cross-comparison with the study performed in Riel et al. (2015) with Cosmo Sky-Med data actually revealed a very good accordance with the TanDEM-X results presented in this study.

## 7. Graben and lava path

For the sake of completeness, and being relevant for further geophysical interpretations, we briefly discuss the changes in the eruptive location, near the northern tip of Vatnajökull glacier in the Holuhraun plain (see Fig. 1). A TanDEM-X image pair acquired on September 09, 2014, serves as a complement to a nominal acquisition acquired at the same incidence angle on November 11, 2011. Also in this case, DEM differencing is the technique used to reveal the dynamical changes of the volcanic system. In particular, the effects of the eruption and the connected processes on the glacier and its foreland are measured in the Holuhraun area. The Holuhraun lava field is clearly visible in the northern part of the image shown in Fig. 11, giving the extent and also the different heights of the lava field on September, 09, 2014. The dyke propagation from the Bárðarbunga caldera to the Holuhraun lava field also had several effects on the surface of the glacier and the foreland. Subsidence of several meters within the graben structure, having a width of up to 1 km, is visible in both, the glaciated area and also north of the glacial rim. Along the path of the dyke propagation over the glacier, several cauldrons with a diameter of hundreds of meters and a subsidence of tens of meters indicate stationary phases in propagation with possible small subglacial effusive events. In addition to the volcanic activity, the end of the glacial tongue shows ablation of several meters along the whole monitored extent.

## 8. Conclusions

The TanDEM-X mission is a useful system in tracking Earth dynamics. In this paper, the focus has been on the particular case of a caldera monitoring, in the Bárðarbunga volcanic system in Iceland, during an ongoing eruptive event. A peculiarity of this caldera is the glacial environment. A study on the DEM accuracy expectations based on the terrain to map, i.e. snow, and the system geometry has been presented. Various physical snow properties have a large impact on the phase center location, measured through the signal penetration depth. For instance, in the analyzed data stack, composed by two summer takes and three autumn ones, the difference in snow wetness brings a discrepancy of some meter in the phase center location, with an elevation value closer to the surface top for summer takes. As a consequence, the results become biased, when not properly taking into consideration the local environment and the system used. For the time periods analyzed, the measured maximum rate of subsidence at the caldera location is about 50 cm/day, in agreement with other independent measurements. The caldera volume loss 69 days after the main eruption started is approximately one cubic kilometer. This value is very close to measurements of the lava volume during the same period. An additional validation has been performed with the help of altimeter elevation profiling over the caldera.

Generally, the topographical mapping with temporal elevation data at a medium-high horizontal resolution of about 10 m provides the opportunity to have a broad view of the imaged test site and to locate

small structures. For instance, structural changes at the northwestern part of the Vatnajökull glacier, such as new cauldron formations and accumulations, are clearly identified, as well as changes in the growth of the lava field and changes along the last segment of the dyke propagation from the caldera. All these quantitative measurements derived with spaceborne bistatic interferometry are particularly relevant for monitoring/civil protection agencies and researchers since they are not easily retrieved with on-site instruments.

## Acknowledgements

Authors would like to acknowledge Thórdís Högnadóttir and Magnús Tumi Gudmundsson for sharing the altimeter data, as well as Eyjólfur Magnússon for discussions on the Bárðarbunga eruption. Authors would also like to thank the anonymous reviewers for their work in revising the paper and improving it over all its aspects. TanDEM-X data are provided by DLR under proposal XTIGLAC6603. Support for this work was received from the European Community's Seventh Framework Programme Grant No. 308377 (Project FUTUREVOLC).

## References

- Albino, F., Smets, B., d'Oreye, N., & Kervyn, F. (2015). High-resolution TanDEM-X DEM: An accurate method to estimate lava flow volumes at Nyamulagira volcano (DR Congo). *Journal of Geophysical Research: Solid Earth*, 120, 4189–4207.
- Amelung, F., Jónsson, S., Zebker, H., & Segall, P. (2000). Widespread uplift and 'trapdoor' faulting on Galapagos volcanoes observed with radar interferometry. *Nature*, 407(6807), 993–996.
- Bamler, R., & Hartl, P. (1998). Synthetic aperture radar interferometry. *Inverse Problems*, 14(4), R1.
- Björnsson, H. (2003). Subglacial lakes and jökulhlaups in Iceland. *Global and Planetary Change*, 35(3), 255–271.
- Colesanti, C., Ferretti, A., Prati, C., & Rocca, F. (2003). Monitoring landslides and tectonic motions with the Permanent Scatterers technique. *Eng. Geol.*, 68(1), 3–14.
- Cuffey, K. M., & Paterson, W. S. B. (2010). *The physics of glaciers*. Academic Press.
- Deo, R., Rossi, C., Eineder, M., Fritz, T., & Rao, Y. S. (2015). Framework for fusion of ascending and descending pass TanDEM-X raw DEMs. Selected topics in applied earth observations and remote sensing. *IEEE Journal of*, 99, 1–9.
- Erten, E., Rossi, C., & Yuzugullu, O. (2015). Polarization impact in TanDEM-X data over vertical-oriented vegetation: The paddy-rice case study. *IEEE Geoscience and Remote Sensing Letters*, 12(7), 1501–1505.
- Fierz, C., Armstrong, R. L., Durand, Y., Etchevers, P., Greene, E., McClung, D. M., & Sokratov, S. A. (2009). The international classification for seasonal snow on the ground. *IHP-VII technical documents in hydrology N83, IACS contribution N1, UNESCO-IHP, Paris* 2009.
- Gatelli, F., MontiGuarnieri, A., Parizzi, F., Pasquali, P., Prati, C., & Rocca, F. (1994). The wavenumber shift in SAR interferometry. *IEEE Transactions on Geoscience and Remote Sensing*, 32(4), 855–865.
- Gertisser, R. (2010). Eyjafjallajökull volcano causes widespread disruption to European air traffic. *Geology Today*, 26(3), 94–95.
- Gíslason, S. R., Stefánsdóttir, G., Pfeffer, M. A., Barsotti, S., Jóhannsson, T., & Goleczka, I. (2015). Environmental pressure from the 2014–15 eruption of Bárðarbunga volcano, Iceland. *Geochemistry Perspectives Letters*, 1, 84–93.
- Gruber, A., Wessel, B., Huber, M., & Roth, A. (2012). Operational TanDEM-X DEM calibration and first validation results. *ISPRS Journal of Photogrammetry and Remote Sensing*, 73, 39–49.
- Gruber, A., Wessel, B., Martone, M., & Roth, A. (2015). The TanDEM-X DEM Mosaicking: Fusion of multiple acquisitions using InSAR quality parameters. Selected topics in applied earth observations and remote sensing. *IEEE Journal of*, 99, 1–9.
- Gudmundsson, M. T., Björnsson, H., & Pálsson, F. (1995). Changes in jökulhlaup sizes in Grímsvötn, Vatnajökull, Iceland, 1934–91, deduced from in-situ measurements of subglacial lake volume. *Journal of Glaciology*, 41(138), 263–272.
- Gudmundsson, M. T., Högnadóttir, P., Kristinsson, A. B., & Guðbjörnsson, S. (2007). Geothermal activity in the subglacial Katla caldera, Iceland, 1999–2005, studied with radar altimetry. *Annals of Glaciology*, 45(1), 66–72.
- Gudmundsson, M. T., Larsen, G., Höskuldsson, Á., & Gylfason, A. G. (2008). Volcanic hazards in Iceland. *Jökull*, 58, 251–268.
- Gudmundsson, M. T., Jónsdóttir, M., & Roberts, K. (2015). The 2014–2015 slow collapse of the Bárðarbunga caldera, Iceland. *Geophysical Research Abstracts*, 17, EGU 2015–12521.
- Hajnsek, I., & Busche, T. (2014). TanDEM-X: Science activities. In *EUSAR 2014; 10th European Conference on Synthetic Aperture Radar; Proceedings of* (pp. 1–3).
- Hallikainen, M. T., Ulaby, F., & Abdelrazik, M. (1986). Dielectric properties of snow in the 3 to 37 GHz range. *IEEE Transactions on Antennas and Propagation*, 34.11, 1329–1340.
- Hooper, A., Segall, P., & Zebker, H. (2007). Persistent scatterer interferometric synthetic aperture radar for crustal deformation analysis, with application to Volcán Alcedo, Galápagos. *Journal of Geophysical Research: Solid Earth* (1978–2012), 112(B7).
- Hooper, A., Prata, F., & Sigmundsson, F. (2012). Remote sensing of volcanic hazards and their precursors. *Proceedings of the IEEE*, 100(10), 2908–2930.

- Ishimaru, A. (1978). *Wave propagation and scattering in random media*. New York: Academic press.
- Jónsson, S., Zebker, H., Cervelli, P., Segall, P., Garbeil, H., Mougini-Mark, P., & Rowland, S. (1999). A shallow-dipping dike fed the 1995 flank eruption at Fernandina volcano, Galapagos, observed by satellite radar interferometry. *Geophysical Research Letters*, 26(8), 1077–1080.
- Johnson, D. J., Sigmundsson, F., & Delaney, P. T. (2000). Comment on “volume of magma accumulation or withdrawal estimated from surface uplift or subsidence, with application to the 1960 collapse of Kilauea volcano” by PT Delaney and DF McTigue. *Bulletin of Volcanology*, 61(7), 491–493.
- Just, D., & Bamler, R. (1994). Phase statistics of interferograms with applications to synthetic aperture radar. *Applied Optics*, 33(20), 4361–4368.
- Krieger, G., Moreira, A., Fiedler, H., Hajnsek, I., Werner, M., Younis, M., & Zink, M. (2007). TanDEM-X: A satellite formation for high-resolution SAR interferometry. *IEEE Transactions on Geoscience and Remote Sensing*, 45(11), 3317–3341.
- Krieger, G., Hajnsek, I., Papathanassiou, K., Eineder, M., Younis, M., De Zan, F., Prats, P., Huber, S., Werner, M., Fiedler, H., et al. (2009). The Tandem-L mission proposal: Monitoring earth's dynamics with high resolution SAR interferometry. *Radar Conference, 2009 IEEE* (pp. 1–6) IEEE.
- Kubanek, J., Westerhaus, M., Schenk, A., Aisyah, N., Brotopuspito, K. S., & Heck, B. (2015). Volumetric change quantification of the 2010 Merapi eruption using TanDEM-X InSAR. *Remote Sens. Environ.*, 164, 16–25.
- Icelandic Met Office (2014). <http://en.vedur.is/earthquakes-and-volcanism/articles/nr/2947>
- Institute of Earth Science (2014). University of Iceland. [http://earthice.hi.is/bardarbunga\\_holuhraun](http://earthice.hi.is/bardarbunga_holuhraun)
- Larsen, G., Gudmundsson, M. T., & Björnsson, H. (1998). Eight centuries of periodic volcanism at the center of the Iceland hotspot revealed by glacier tephrostratigraphy. *Geology*, 26(10), 943–946.
- Larsen, G., Gudmundsson, M. T., Einarsson, P., Óladóttir, B. A., & Thordarson, T. (2015). The Bárðarbunga central volcano, crustal structure and eruption history. In: *EGU General Assembly Conference*, 17. (pp. 11322).
- Mätzler, C., & Wegmüller, U. (1987). Dielectric properties of freshwater ice at microwave frequencies. *Journal of Physics D: Applied Physics*, 20, 12.
- Magnússon, E. (2015). *Personal communication*.
- Old, G. H., Lawler, D. M., & Snorrason, Á. (2005). Discharge and suspended sediment dynamics during two jökulhlaups in the Skaftá river, Iceland. *Earth Surface Processes and Landforms*, 30(11), 1441–1460.
- Poland, M. P. (2014). Time-averaged discharge rate of subaerial lava at Kilauea Volcano, Hawaii, measured from TanDEM-X interferometry: Implications for magma supply and storage during 2011–2013. *Journal of Geophysical Research - Solid Earth*, 119(7), 5464–5481.
- Rabus, B., Eineder, M., Roth, A., & Bamler, R. (2003). The shuttle radar topography mission—A new class of digital elevation models acquired by spaceborne radar. *ISPRS Journal of Photogrammetry and Remote Sensing*, 57(4), 241–262.
- Richards, J. A. (2009). *Remote sensing with imaging radar*. Heidelberg-Springer.
- Riel, B., Milillo, P., Simons, M., Lundgren, P., Kanamori, H., & Samsonov, S. (2015). The collapse of Bárðarbunga caldera, Iceland. *Geophysical Journal International*, 202(1), 446–453.
- Rignot, E., Echelmeyer, K., & Krabill, W. (2001). Penetration depth of interferometric synthetic-aperture radar signals in snow and ice. *Geophysical Research Letters*, 28(18), 3501–3504.
- Rossi, C., Gonzalez, F. R., Fritz, T., Yague-Martinez, N., & Eineder, M. (2012). TanDEM-X calibrated raw DEM generation. *ISPRS Journal of Photogrammetry and Remote Sensing*, 73, 12–20.
- Rossi, C., & Erten, E. (2015). Paddy-rice monitoring using TanDEM-X. *IEEE Transactions on Geoscience and Remote Sensing*, 53(2), 900–910.
- Rossi, C., & Eineder, M. (2015). High-resolution InSAR building layovers detection and exploitation. *IEEE Transactions on Geoscience and Remote Sensing*, 53(12), 6457–6468.
- Rott, H., Floricioiu, D., Wuite, J., Scheiblauer, S., Nagler, T., & Kern, M. (2014). Mass changes of outlet glaciers along the Nordensjoköld Coast, northern Antarctic Peninsula, based on TanDEM-X satellite measurements. *Geophysical Research Letters*, 41(22), 8123–8129.
- Schlund, M., von Poncet, F., Hoekman, D. H., Kuntz, S., & Schullius, C. (2014). Importance of bistatic SAR features from TanDEM-X for forest mapping and monitoring. *Remote Sensing of Environment*, 151, 16–26.
- Sigmundsson, F., Hreinsdóttir, S., Hooper, A., Arnadóttir, T., Pedersen, R., Roberts, M., Óskarsson, N., Auriac, A., Decriem, J., Einarsson, P., et al. (2010). Intrusion triggering of the 2010 Eyjafjallajökull explosive eruption. *Nature*, 468(7322), 426–430.
- Sigmundsson, F., Hooper, A., Parks, M., Spaans, K., Gudmundsson, G., Drouin, V., Samsonov, S., White, R., Hensch, M., Pedersen, R., et al. (2015). Segmented lateral dyke growth in a rifting event at Bárðarbunga volcanic system, Iceland. *Nature*, 517, 191–195.
- Stevenson, J. A., Loughlin, S., Rae, C., Thordarson, T., Milodowski, A. E., Gilbert, J. S., ... Ártung, U. (2012). Distal deposition of tephra from the Eyjafjallajökull 2010 summit eruption. *Journal of Geophysical Research: Solid Earth* (1978–2012), 117(B9).
- Stiles, W. H., & Ulaby, F. T. (1980). The active and passive microwave response to snow parameters: 1. Wetness. *Journal of Geophysical Research, Oceans*, 85(C2), 1037–1044 (1978–2012).
- Tómasson, H. (1996). The jökulhlaup from Katla in 1918. *Annals of Glaciology*, 22, 249–254.
- Thordarson, T., & Self, S. (2003). Atmospheric and environmental effects of the 1783â€”1784 Laki eruption: a review and reassessment. *Journal of Geophysical Research: Atmospheres* (1984–2012), 108(D1).
- Touzi, R., Lopes, A., Bruniquel, J., & Vachon, P. W. (1999). Coherence estimation for SAR imagery. *IEEE Transactions on Geoscience and Remote Sensing*, 37(1), 135–149.
- Taubenböck, H., et al. (2012). Monitoring urbanization in mega cities from space. *Remote Sensing of Environment*, 117, 162–176.
- Williams, R. S., Jr., Hall, D. K., & Benson, C. S. (1991). Analysis of glacier facies using satellite techniques. *Journal of Glaciology*, 37(125), 120–128.
- Zebker, H. A., & Villasenor, J. (1992). Decorrelation in interferometric radar echoes. *IEEE Transactions on Geoscience and Remote Sensing*, 30(5), 950–959.
- Zhong, L., & Dzurisin, D. (2014). InSAR imaging of Aleutian volcanoes: Monitoring a volcanic arc from space. *Springer Science and Business Media*.